Exploring the electron density in plasma induced by EUV radiation: II. Numerical studies in argon and hydrogen

D.I. Astakhov,[1] W.J. Goedheer,[2] C.J. Lee,[1] V.V. Ivanov,[3] V.M. Krivtsun,[3] K.N. Koshelev,[3] D.V. Lopaev,[4] R.M. van der Horst,[5] J. Beckers,[5] E.A. Osorio,[6] and F. Bijkerk[1]

[1]*XUV Group, MESA+ Institute for Nanotechnology, University of Twente, P.O. Box 217, 7500 AE Enschede, The Netherlands*
[2]*FOM Institute DIFFER - Dutch Institute for Fundamental Energy Research, PO Box 6336, 5600HH Eindhoven, the Netherlands, The Netherlands*
[3]*Institute for Spectroscopy RAS (ISAN), Fizicheskaya 5, Troitsk 142190, Russian Federation*
[4]*Skobeltsyn Institute of Nuclear Physics, Lomonosov Moscow State University, Leninskie Gory, Moscow 119991, Russian Federation*
[5] *Department of Applied Physics, Eindhoven University of Technology, PO Box 513, 5600MB Eindhoven, The Netherlands*
[6] *ASML The Netherlands B.V., PO Box 324, 5500AH Veldhoven, The Netherlands*

We used numerical modeling to study the evolution of EUV-induced plasmas in argon and hydrogen. The results of simulations were compared to the electron densities measured by microwave cavity resonance spectroscopy. It was found that the measured electron densities can be used to derive the integral amount of plasma in the cavity. However, in some regimes, the impact of the setup geometry, EUV spectrum, and EUV induced secondary emission should be taken into account. The influence of these parameters on the generated plasma and the measured electron density is discussed.

arXiv:1603.08130v1 [physics.plasm-ph] 26 Mar 2016

I. INTRODUCTION

In the semiconductor industry, the photolithography process is used to create patterns on silicon wafers, an important step in microchip production. Due to diffraction, the characteristic pattern dimensions depend on the illuminating wavelength. However, it is becoming increasingly complicated to further reduce printed feature sizes with deep ultraviolet (DUV) light sources. As a result, extreme ultraviolet (EUV) lithography, operating at a wavelength of 13.5 nm, is expected to be used to print integrated circuits with very high resolution features.

For various reasons, a buffer gas is frequently used in both laboratory and industrial EUV light sources. However, even at low pressure (1 .. 30 Pa), EUV absorption leads to EUV induced plasma formation. There is a strong need for reliable diagnostics of EUV induced plasmas, because the interaction of an EUV induced plasma with the chamber interior and optical elements can lead to various plasma induced processes, such as surface etching, accelerated deposition of overlayers, and oxidation, depending on the exact constituents of the background gas [1, 2].

It was shown in [3] that it is possible to measure the electron density of an EUV induced plasma, at relevant background gas pressures, by measuring the resonant frequency shift of a microwave cavity that contains the plasma. Although this is a highly sensitive method, it only allows the field average [4] electron density inside the cavity to be determined.

Nevertheless, it is interesting to know the spatial distribution of plasma in the cavity, the electron temperature and other plasma parameters. Unfortunately, measuring all the relevant parameters experimentally is difficult due to the transient nature of the EUV induced plasma. For example, the insertion of a probe can yield unreliable estimates of plasma parameters for EUV induced plasmas, since, during and after the EUV pulse, the probe signal is heavily distorted [5, 6].

In this paper, we use a particle-in-cell model of the EUV-induced plasma to determine the spatio-temporal distribution of the electron density, the electron-ion balance, and the influence that some confounding factors may have on the spatio-temporal distribution of the plasma. Specifically, we studied how the changes in buffer gas, EUV intensity, EUV spectrum, and secondary electron emission change the plasma in the cavity.

We found that the EUV-induced plasma can be in a distinct “charged” regime. In this regime (as opposed to the quasi neutral regime, that corresponds to usual plasmas, such as glow discharges) the quasi neutrality is violated everywhere in the plasma. This regime forms due to the escape of fast photoelectrons from the plasma to the cavity walls. That leaves a highly charge imbalanced plasma. Such a plasma is not well suited for study with the microwave cavity method. However, it happens that such a regime is on the lower boundary of the methods sensitivity. Therefore, it can be easily detected and avoided.

We evaluated the accuracy of the simulations by comparing of the simulated field averaged electron density with the experimentally measured electron densities. We show that in the quasi-neutral plasma regime, the microwave cavity resonance shift provides an accurate tool for estimating plasma parameters, using only the spatial profile of the cavity mode and the EUV beam profile as input factors. In the charged regime, similar accuracy can only be obtained if on has knowledge of the EUV spectrum and secondary electron emission among other factors.

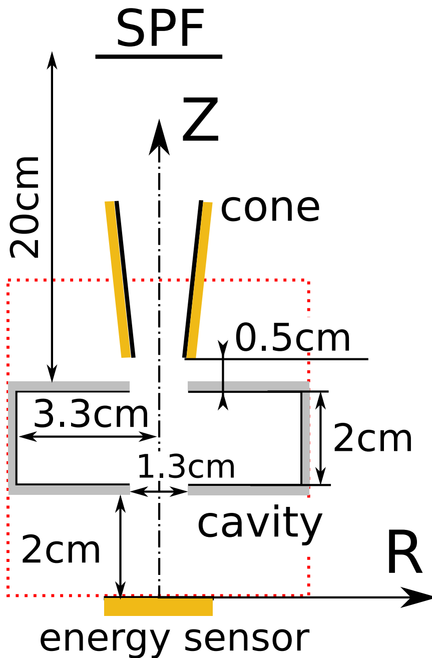

Figure 1: Configuration of the experimental chamber. The EUV radiation is introduced via a spectral purity filter (SPF) along the symmetry axis of the cavity.

II. EXPERIMENT

The experimental setup is described in detail in Ref. [3]. Therefore, here, we provide a minimal outline of the experimental procedure.

The plasma is ignited in a resonant cavity (see Fig. 1) by a beam of EUV radiation, which is introduced along the axis of the cylindrically symmetric cavity with an aperture and beam guide to prevent residual EUV from being incident on the cavity walls. The EUV radiation is produced by a xenon based discharge source and propagated through a spectral purity filter (SPF) to limit the spectrum to photon energies to the range of 70 to 120 eV. The spectrum of the source after transmission through the SPF is shown in Fig. 2.

The EUV power is monitored using a sensitive thermocouple, attached to a copper disk, located approximately 2 cm behind the cavity.

As described earlier, the average electron density in the resonant cavity was determined by measuring the resonant frequency of the microwave cavity (see [3] for details).

III. MODEL

The dynamics of the EUV-induced plasma was simulated using a two dimensional (rz cylindrically symmetric) particle-in-cell plasma model with Monte Carlo collisions (PIC-MC). Both electrons and ions are represented by particles to describe the dynamics of the plasma accurately. The model follows the general PIC scheme, described elsewhere [7].

A. Photoionization

The absorption of EUV radiation in the volume is included as a source of slow ions and fast electrons. To simulate photoionization, we use the measured spatial (axially averaged) and temporal profiles of the EUV pulse (see Fig. 5 and Fig. 9). We assume that the spatial profile and spectrum of the EUV source does not vary during EUV pulse.

The spatial and temporal coordinates of electron-ion pairs that are created by ionization events are added to the simulation domain using a probability distribution function that is weighted by the spatial and temporal profiles of the EUV pulse. The energy of the injected electrons is set to the difference between the photon energy, which is selected according to the EUV spectrum, and the ionization potential of the gas species (H_2 or Ar). The the power spectral density of the EUV beam is recalculated along the z axis to take into account absorption by the gas between SPF and cavity entrance using the Lambert–Beer law.

The electrons are emitted preferentially in the r plane, with a distribution function

$$P(\theta) \sim 1 - \beta\frac{1}{4}(3\cos^2\theta - 1) \tag{1}$$

where θ is the angle between electron velocity and EUV beam direction and β is the anisotropy factor. This form of angular distribution corresponds to photoionization by unpolarized light [8]. For hydrogen we use $\beta = 2$, as this agrees with experiments in the energy range of the measurements. For argon, we use data from [9, 10] for photon energies below 95 eV, and $\beta = 1.3$ above 95 eV.

The energy dependent photoionization cross-sections are taken from [11] and [12] for H_2. For argon there are several measurements (e.g. [13], [14] and [15]). We followed the recommendation of [16] and used data from [13] for the total absorption cross-section. The cross-section for photoionization to Ar^{++} is taken from [17].

B. EUV the spectrum

To simulate the EUV plasma ignition, the spectrum of the EUV radiation must be taken into account. Unfortunately there is no simple experimental method to control the radiation spectrum in the relevant broad range of VUV to EUV photon energies (15.4 – 120 eV).

Therefore, as input for the simulations, we have used the source spectrum, measured before transmission through the SPF, convolved with the measured transmis-

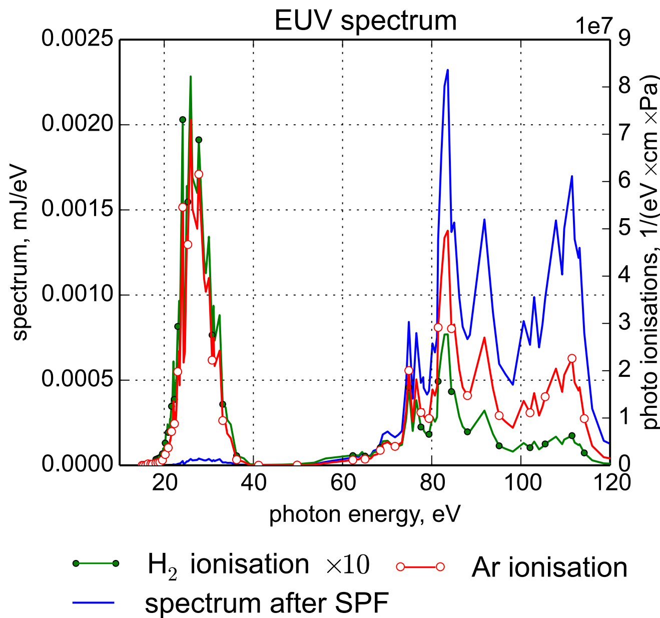

Figure 2: EUV power spectral density ($I(E)$)spectrum as used in the simulations. The right axis shows the number of direct photoionization events due to transmission of 0.044 mJ EUV through 1 Pa of gas, i.e. $I(E) \cdot N[1\text{Pa}] \cdot \sigma(E)/E$, where, $\sigma(E)$ is the photoabsorption cross-section, E, the photon energy, and $N[1Pa]$ the number density .

sion spectrum of the Si:Zr SPF. This results in the EUV spectrum shown in Fig. 2.

Fig. 2 shows that the transmission of the SPF filter in the 20 - 40 eV range, which is in the range of 1% of the total pulse energy, results in significant additional photoionization. This additional photoionisation is comparable to the direct photoionization due to the high energy part of the spectrum (i.e. $60-120$ eV), because the photo absorption cross-section is very large in the 20 - 40 eV range compared to the $60-120$ eV range.

Although the presence of the radiation in the 20 – 40 eV range has been confirmed by measurements, the absolute accuracy of the transmitted spectrum is not accurately known. This introduces an additional uncertainty into the simulations. Because the accuracy of the measurements of the EUV dose per pulse is also not know, we choose to keep spectrum shape constant and vary the EUV dose. This approach has the advantage that the integral accuracy of the simulations can be estimated by the difference between the measured EUV energy per pulse and that required for good agreement between experiments and simulations for both gases (i.e., we require that the same EUV power results in agreement between model and experiment over a range of experimental conditions).

C. Secondary electron emission and influence of chamber configuration

Emission of slow electrons from the walls to the plasma due to any reason can significantly decrease the plasma potential, or even lead to the collapse of the plasma sheath [18] leading to effective energy transfer from the electrons to the walls. Therefore, it is important to take into account secondary electron emission (SEE) from the the surfaces that are exposed to the plasma.

For the considered setup, energy is only injected into the plasma during the EUV pulse via photoionization and photoelectrons emission from irradiated surfaces. Therefore, the decrease of the plasma potential or sheath collapsed due to SEE can result in significant loss of fast electrons to the walls. Hence, the maximum number of ionization events also decreases.

1. *Secondary electron emission*

In order to estimate the role of emission from the aluminum cavity walls due to electron impact, we have considered three cases. The first corresponds to no secondary electron or ion induced emission from the walls. In the second case, electron emission due to both electron and ion impact is taken into account. The data for aluminum shows a significant spread of possible emission yields. Nevertheless, for the energy range of primary photoelectrons (e.g. $50-75$ eV) the reported values are typically larger than 0.3 [19, 20] so we use the yield reported for clean aluminum in Ref. [20].

The yield also significantly depends on the surface conditions. For aluminum with a native oxide, the emission yield [21] is significantly higher than for pure aluminum and corresponds to the yields found for dielectric materials [22, 23]. Therefore, in the third case, the yield for aluminum with a native oxide is used. The yield is estimated from Ref. [21] for energies below 25 eV, and extrapolated linearly for energies above 25 eV.

We do not discriminate between backscattered electrons and true secondary electrons, because, for our study, only the total flux from the surface is important. In the model, we assume that most of the emitted electrons are cold, i.e. they have a significantly lower energy compared to the energy of the impacting electrons. However, for electron with energies below 10 eV this approximation is not valid, due to the higher probability of elastic backscattering. But, these backscattered electrons do not have sufficient energy to ionize more of the background gas, if not accelerated by a plasma potential. Therefore, the additional error due to this approximation is expected to be small.

2. influence of chamber configuration

The configuration of the experimental setup is presented in Fig. 1. The SPF filter, copper cone and copper disc of energy sensors emit secondary electrons under EUV irradiation. But, these electrons do not contribute directly to the ionization inside cavity, because the number of high energy secondaries is small and the electron flux is not focused.

To estimate the influence of this effect, we have simulated two geometrical configurations: a large volume, which includes the cone and disc (the dotted rectangle in Fig. 1), and a small volume, which includes only the cavity with periodic boundary conditions at the cavity openings. We have not included the full length of the cone and SPF into simulations, because the aspect ratio of the cone diameter to length is very small (i.e. 0.05).

3. Photo electron emission from surface

In order to model the configuration that includes the cone and copper disc, photoelectron emission should be taken into account. The energy spectrum of photoelectrons emitted from the copper disk and cone surfaces are calculated from [24]:

$$P(E) \sim \frac{E}{(E+W)^4} \tag{2}$$

Here $P(E)$ is the probability of emitting an electron with energy, E, from a surface with a work function, W. For copper $W = 5$ eV [25]. For electrons emitted from the surface, we assume an angular dependence given by a cosine emission law [24]. The effective photoelectron yield from copper was set to 0.05 electron/photon [26].

D. Grid resolution

The grid resolution was chosen to resolve the Debye length. To estimate the minimum Debye radius in simulations, we assumed a temperature of 0.5 eV and an estimated maximum plasma density. The maximum plasma density was estimated from direct photoionization (i.e., Fig. 2), increased by the maximum possible number of impact ionizations that the primary electrons could generate, i.e., for a 90 eV photon, the photoelectron has an energy of 74.6 eV, therefore, the maximum number of ions produced by that electron is 5, increasing the plasma density by a factor of 5. Note, however, that, in the simulation, the contribution of fast photoelectrons is significantly smaller due to the contribution of inelastic collisions, and that many photoelectrons escape to the wall before generating the maximum number of ions.

E. Cross-sections sets

Two independent cross-section sets are used for modelling hydrogen and argon. Both sets consists of electron and ion collisions with corresponding neutrals. The collisions between plasma species and three body processes are neglected due to their low probability under the conditions considered here.

We make use of the procedure described in [27] to perform Monte Carlo collisions with the background gas. We tested the consistency of our implementation by modeling swarm experiments and found good agreement with experimental values [28] for the first Townsend electron ionization coefficient, the electron mobility, for H^+ and H_3^+ mobility in hydrogen [29], and for Ar^+ and Ar^{++} mobility in argon [30, 31].

1. Hydrogen

To accurately model electron collision related processes in hydrogen discharges with a Monte Carlo (MC) model, one needs to take into account the differential cross-sections for ionization and excitation processes. As described in detail in [32], the particular choice of the angular dependence of cross-sections significantly influences the simulation results.

For electron $-$ H_2 collisions we adopt a set of cross sections found in Ref. [32] with small corrections. We use an experimentally determined doubly differential cross-section for the electron impact ionization of hydrogen [33, 34]. Electron elastic scattering and hydrogen electronic excitations, and angular scattering data taken from [35].

The set of cross-sections for collisions between ions and hydrogen is based on [36] because this set provides good agreement with swarm data for ions in hydrogen.

We neglect the formation of H^-, because the cross-section of dissociative electron attachment is very low, and the density of vibrationally excited hydrogen molecules too low to significantly contribute to the production of H^-.

2. Argon

For electron $-$ Ar collisions we adopt a set of cross-sections found in Ref. [37, 38]. We add electron impact ionization of Ar to Ar^{++} from Ref. [39] to the cross-sections set. We use differential cross-section data for electron impact ionization from Ref. [40]. The data from Ref. [40] covers incident electron energy range $17 - 30$ eV. To the authors knowledge there is no systematic differential ionization cross-section measurements for incident electrons in the energy range of $30 - 100$ eV. Hence, for energy range above 30 eV, we use empirical formulas from Ref. [41].

We neglect ionization via the metastable argon exited state. The density of metastables produced in one

EUV pulse is comparable to the plasma density (e.g. $\sim 10^9 - 10^{10}$ 1/cm^3). The maximum of cross-section for electron impact ionization of the metastable argon exited state is approximately 10^{-15} 1/cm^2 [42]. Therefore, the maximum corresponding ionization frequency can estimated as $\nu_i = n\sigma v \sim 2 \cdot 10^3$ 1/s. The simulated plasma evolution is less than 10 μs, yielding an upper bound of 0.02 ionization events per electron for the step wise ionization. This is negligible compared to the direct EUV ionization and ionization by fast photoelectrons. Moreover, there is no pulse-to-pulse accumulation because the time between EUV pulses is larger than metastable's lifetime due to quenching on the chamber walls.

The set of cross-sections for collisions between Ar^+ and argon is based on [43]. For collisions between Ar^{++} and argon we use data from [44].

F. Calculation of the field average electron density

In order to compare the model results with experimental measurements, the simulated spatially-resolved electron density was averaged over the spatial profile of the resonant microwave cavity mode as follows.

$$\langle n_e \rangle = \frac{\int n_e \vec{E}^2 dV}{\int \vec{E}^2 dV} \quad (3)$$

The magnitude of the microwave field was very small (mV range), therefore, it was not included in PIC-MC simulations.

IV. RESULTS AND DISCUSSION

The ignition and decay of the EUV induced plasma was simulated for a series of argon and hydrogen pressures (i.e. 1 Pa, 5 Pa, 10 Pa) to compare with experimental results. The best agreement with experiments for both gases and all considered pressures was obtained in simulations where we have included the larger chamber configuration, and used a spectrum that includes a VUV contribution. The comparison between simulated field averaged electron density and experimental measurements is presented in Fig. 3 and Fig. 4.

In these simulations, we have decreased the EUV energy per pulse to 0.035 mJ/pulse from the experimentally measured value of 0.044 mJ/pulse. This difference, in combination with $\sim$ 20% relative errors for the field averaged electron densities (i.e. in Fig. 3 and Fig. 4), yields a $\sim$ 50% cumulative uncertainty, which is comparable to the $\sim$30% error margin of of the experiment [3].

A. Relation of field averaged electron density and simulated values

The cavity method allows the field averaged electron density to be determined. But, the relationship of this

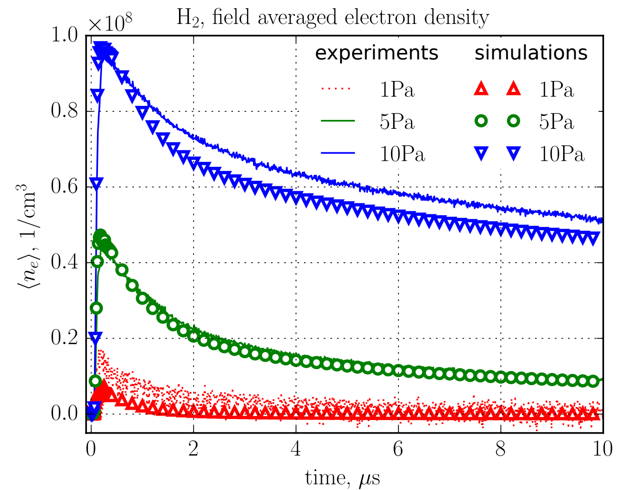

Figure 3: Comparison between the simulated (symbols) and measured (lines, data from part I) time dependence of field averaged electron densityfor 1 (red), 5 (green), and 10 (blue) Pa hydrogen.

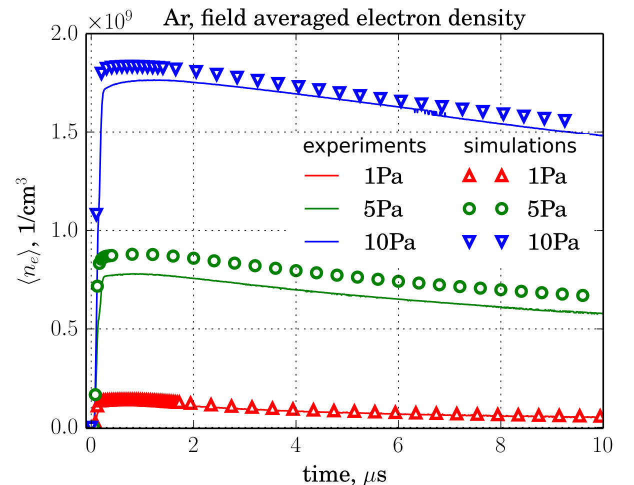

Figure 4: Comparison between the simulated (symbols) and measured (lines, data from [45]) time dependence of field averaged electron density for 1 (red), 5 (green), and 10 (blue) Pa argon.

quantity to the actual plasma density is not straightforward. During the first 1 μs, the simulated plasma is much denser than that measured by the cavity. However, as the plasma expands, the difference between simulated plasma density and cavity measurements becomes smaller. For 5 Pa H_2 at 10 μs, the ratio between the simulated plasma density and that measured by the cavity is only about a factor of two (see Fig. 5).

Nevertheless, the plasma density measured by the cavity is very useful to estimate the amount of the plasma in the cavity. Let us define the effective volume of

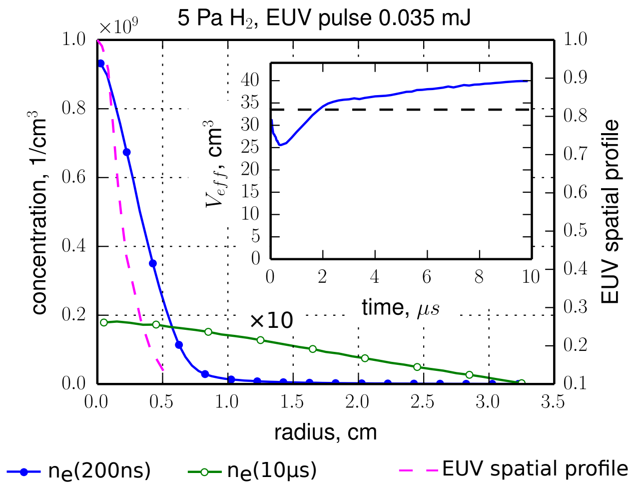

Figure 5: Radial distributions of electron density in the cavity for 5 Pa H_2 and the EUV spatial profile that was used for all simulations. The insert shows the time dependence of the effective volume probed by the microwave mode. The simulated volume is a solid blue line, while the dashed black line corresponds to analytical estimation (see text).

the cavity as ratio of the full number of electrons in the cavity to the cavity measured electron density i.e. $V_{eff} = \int n_e dV / \langle n_e \rangle$. In simulations, this quantity varies only by about a factor of two during the 10 μs simulation window (see insert in Fig. 5). Moreover, the estimation of the effective volume, based on the EUV spatial profile (as an approximation to the EUV plasma distribution), and the spatial profile of the microwave cavity mode (see Part I) agree well with the simulated values (dashed black line in the insert in Fig. 5)

Therefore, the amount of EUV induced plasma can be estimated from the measured cavity response with a relative accuracy of about 30%. Hence, the amount of absorbed radiation can be estimated with similar accuracy, if the other factors (see below) that effect plasma formation are eliminated.

The simulated evolution of the effective volume is non monotonic in time. A similar effect was observed in experiments via the ratio of the electron densities measured using 010 and 110 cavity modes [46]. However, in simulations, the decrease of the effective volume just after the EUV pulse is caused by the convolution of the plasma density with the spatial profile of the microwave mode in the cavity.

B. Effect of VUV part of the spectrum

As discussed in section III B, the EUV spectrum after passing through the SPF (see Fig. 2) has two distinct regions: a low energy (20 – 40 eV) VUV part, and a high energy (60 – 120 eV) EUV part. Our simulations show that the VUV contribution is needed to produce consistent results for both gases with the same amount of the radiation dose per pulse. This is because the average number of ionization events per absorbed photon can be larger than one if the emitted fast photoelectron produces addition ionization events.

In our simulations, the average number of ionizations per absorbed EUV photon was observed to be approximately one for H_2 and two for Ar. To obtain the observed electron densities without including ionization due to VUV, the EUV pulse energy must be increased and set to different values for argon and hydrogen.

C. Effect of secondary electron emission due to EUV radiation

Our simulations of the larger, more complete geometry shows that electron emission from the cone walls and copper disk change of the plasma potential. The large EUV induced secondary electron emission from the copper disk leads to the formation of the space charge potential well during EUV pulse, see Fig. 6. The electron current during the pulse on the symmetry axis of the system is directed from the copper disk towards the cavity, thus replacing a large portion of the fast electrons that reach cavity walls. A comparison between the potential in the cavity for 5 Pa H_2 for both geometrical configurations is presented in Fig. 7. For these simulations, the electron induced electron emission from cavity walls was set to zero.

Interestingly, the average electron density decreases for argon gas, but increases for hydrogen, compared to simulations of the cavity only. In the case of hydrogen, the plasma potential is smaller than for argon, due to a lower plasma density. That, in turn, leads to a significant loss of electrons to the cavity walls. Electrons emitted from the cone and copper disc are accelerated into the plasma, compensating for a fraction of the escaped electrons and increase the electron density.

In contrast to hydrogen, the argon plasma is significantly denser, due to the order of magnitude larger absorption of EUV for the same pressure (see Fig. 2). Hence, for argon, the relative charge imbalance between electrons and ions is much smaller than for hydrogen. Therefore, these electrons change the potential landscape of the plasma, increasing the probability of fast photoelectrons escape to the walls and reducing the average number of ionizations per fast electron.

D. Influence of electron induced secondary emission from cavity walls

As discussed in section III C 1 one can expect a significant secondary electron emission yield from the cavity walls under electron impact. However, the inclusion of this effect in the simulations has a small impact on the plasma formation in the cavity (below 5% for the field averaged electron density).

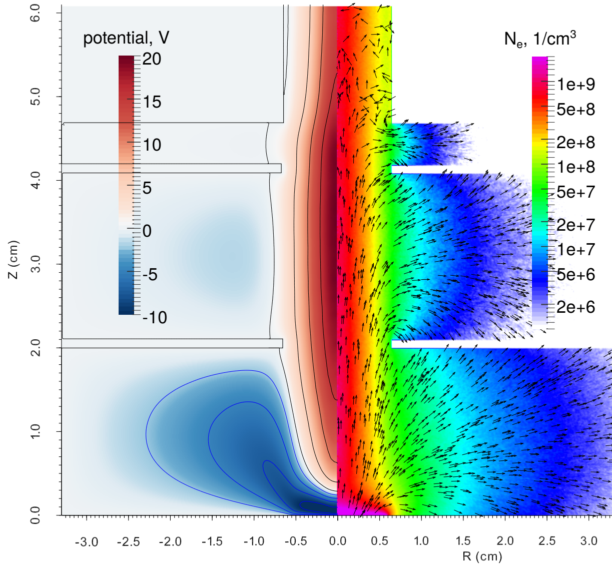

Figure 6: Distribution of the potential, electron density and current direction in the simulation domain 100 ns (see Fig. 9), 5 Pa H_2. The arrows shows the direction of the electron current. The electrons are drained from the copper disc (Z ∼0) into the cavity, leading to a decrease of the plasma potential (see Fig. 7).

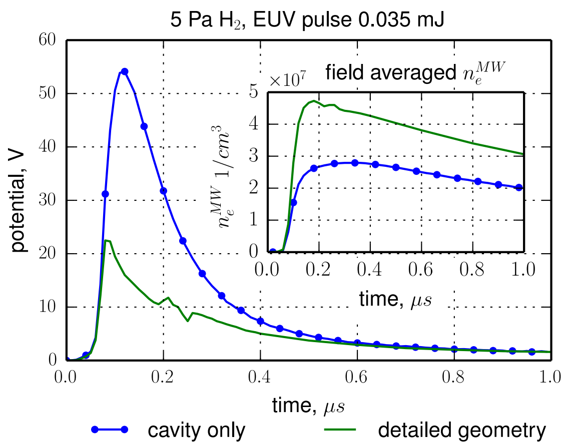

Figure 7: Comparison of the potential in the center of the cavity as function of time for 5 Pa H_2. The large geometrical configuration includes secondary electron emission from the energy sensor, which leads to a decrease of the potential in the cavity. A comparison between the field averaged electron densities in the cavity is shown in the insert. A non-monotonic decrease of the plasma potential for the large configuration is related to SE emission from energy sensor and charge redistribution in the cavity. During the EUV pulse, SE emission leads to a significant decrease of the plasma potential, since the emitted SE electrons replace the escaped primary photoelectrons. Just after the EUV pulse there are no SEs emitted, but some fast photoelectrons are still present in the plasma, therefore, once these fast electrons escape to the walls the plasma potential increases temporally.

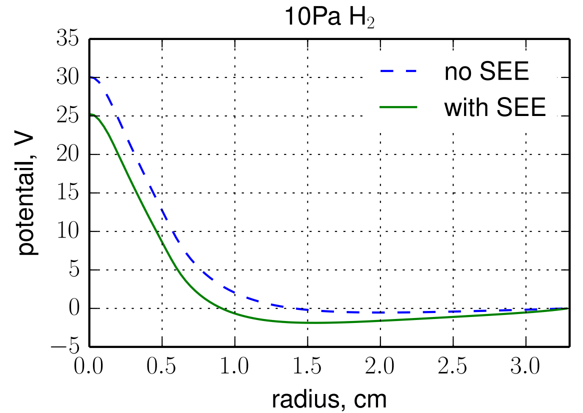

Figure 8: Comparison of the radial dependence of the plasma potential at the center of the cavity with (green) and without SEE (blue) for 10 Pa H_2 at 80 ns after pulse start.

It is explained by changes in the plasma potential (see Fig. 8). Most ionization occurs in the region corresponding to the EUV beam. Electrons that escape from the plasma to the region between the beam and the cavity walls encounter the slow electrons produced on the cavity walls due to electron impact emission. That lead to formation of a local minimum in the plasma potential.

Hence, the potential barrier that electrons in the beam need to overcome in order to escape is similar for both simulations that include and neglect electron induced emission from the cavity wall. Moreover, the potential near cavity wall during the pulse prevents the emitted secondary electron from entering the plasma, thus significantly limiting the influence of SEE on the plasma formation.

E. High charge imbalance plasma for 1Pa H_2

Interestingly, results for 1 Pa H_2, even with inclusion of the VUV part of spectrum, show a significant charge imbalance between ions and electron. Due to the low H_2 pressure, the absorption of EUV radiation is low. The generated plasma has a peak density in the range of $2 \cdot 10^8 - 3 \cdot 10^8$ 1/cm^3, see Fig. 10. This plasma can generate only a low plasma potential, that is not enough to confine high energy primary photoelectrons. As result, after the EUV pulse, a significant fraction of electrons leaves the plasma.

The ratio of the ion density to the sum of the ion and electrons densities as a function of time are presented in Fig. 9. For all simulated cases, in the beginning of the pulse, many fast electrons leave the plasma, creating an excess of ions. After the pulse, the simulation show that the plasma returns to quasi-neutrality (i.e. $n_i/(n_i+n_e) \sim 0.5$), except for the case of 1 Pa H_2 . In the case of 1 Pa, the generated plasma remains significantly charged,

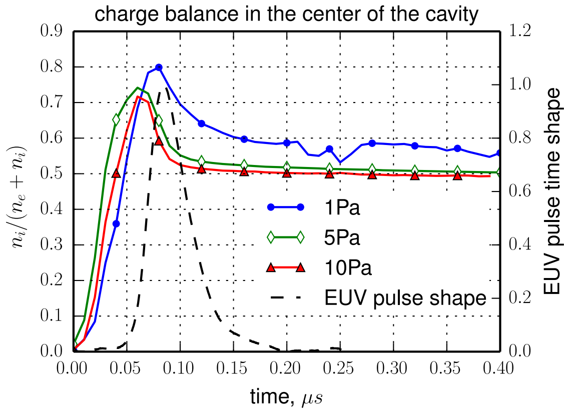

Figure 9: Evolution of the charge balance in the center of the cavity for the case of H_2. The charge imbalance for the case of 1 Pa H_2 lasts significantly longer compared to other cases.

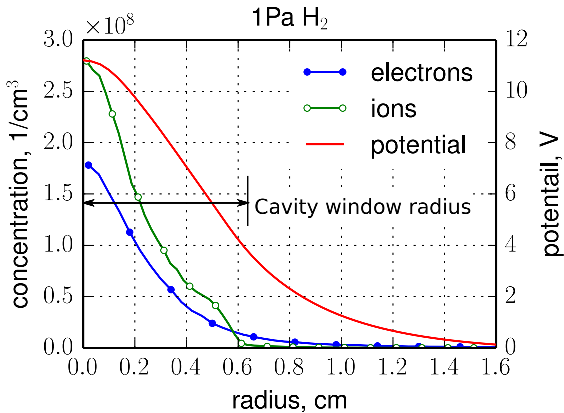

Figure 10: Radial distribution of electrons and ions in the center of the cavity at 150 ns after EUV pulse start.

which leads to a faster decay, due to Coulomb repulsion on the time scale of 1 μs.

V. CONCLUSION

We simulated the evolution of an EUV induced plasma in a microwave resonant cavity. During simulations we observed that the cavity measured electron density can be used to estimate the integral amount of ionization in the cavity.

We show that these estimates are reasonably accurate ($<$ 30% for the considered conditions). This is even the case for estimates that use only the spatial mode profile of the microwave cavity mode and the EUV spatial beam profile. Therefore, a suitable microwave cavity can be used as a valuable diagnostics tool for EUV induced plasmas.

However, the cumulative uncertainties of the SPF transmission and the possible error margin in the measurements of the EUV source spectrum are important for the analysis of EUV plasma formation in hydrogen and argon. This is due to the rapid increase of the absorption cross-section with decreasing photon energy. Even 1% transmission of the SPF filter in the range of 20 – 30 eV has a significant effect on the EUV plasma formation. Moreover, the same spectral range is very important for surface chemistry processes, because the photoabsorption cross-sections are typically very large (e.g. the convolution of the cross-section with the spectrum can be similar for in-band EUV and out-of-band VUV).

The effect of VUV is likely to be significant, because most laboratory sources are discharge based with grazing incidence collector optics, which, without special care will have a significant amount of VUV. Therefore, in laboratory experiments, the EUV spectrum should be measured after the SPF filter, otherwise the remaining VUV radiation can induce a substantial systematic error.

Last but not least, it is important to take into account the EUV (or VUV) induced secondary electron emission (SE) form cavity and/or surroundings. This emission changes the potential distribution in the cavity and, hence, changes the generated plasma density, which further complicates the analysis of the cavity response.

Nevertheless, in case the radiation spectrum and secondary electron emission are known through additional measurements, the microwave cavity response may prove to be a very accurate tool for estimating plasma parameters and related phenomena.

Acknowledgements

This work is part of the research programme 'Controlling photon and plasma induced processes at EUV optical surfaces (CP3E)' of the 'Stichting voor Fundamenteel Onderzoek der Materie (FOM)', which is financially supported by the 'Nederlandse Organisatie voor Wetenschappelijk Onderzoek (NWO)'. The CP3E programme is co-financed by Carl Zeiss SMT and ASML. The authors also acknowledge support from the Province of Overijssel, PANalytical, DEMCON, Solmates, and the University of Twente through the programme of the Industrial Focus Group XUV Optics.

---

[1] Theodore E. Madey, Nadir S. Faradzhev, Boris V. Yakshinskiy, and N.V. Edwards. Surface phenomena related to mirror degradation in extreme ultraviolet (EUV) lithography. *Applied Surface Science*, 253(4):1691–1708,

2006. doi:10.1016/j.apsusc.2006.04.065.

[2] David J. Davis, Georgios Kyriakou, Robert B. Grant, Mintcho S. Tikhov, and Richard M. Lambert. Toward the In Situ Remediation of Carbon Deposition on Ru-Capped Multilayer Mirrors Intended for EUV Lithography: Exploiting the Electron-Induced Chemistry. *The Journal of Physical Chemistry C*, 111(33):12165–12168, 2007. doi:10.1021/jp074766y.

[3] R. M. van der Horst, J. Beckers, S. Nijdam, and G. M. W. Kroesen. Exploring the temporally resolved electron density evolution in extreme ultra-violet induced plasmas. *Journal of Physics D: Applied Physics*, 47(30):302001, July 2014. doi:10.1088/0022-3727/47/30/302001.

[4] S. Gundermann, D. Loffhagen, H.-E. Wagner, and R. Winkler. Microwave diagnostics of the electron density in molecular mixture plasmas. *Contributions to Plasma Physics*, 41(1):45–60, 2001.

[5] van der MHL (Marc) Velden, GMW (Gerrit) Kroesen, van der JJAM (Joost) Mullen, JHJ (Roel) Moors, and Technische Universiteit Eindhoven. *Radiation generated plasmas:a challenge in modern lithography*. PhD thesis, Technische Universiteit Eindhoven, 2008.

[6] A Dolgov, O Yakushev, A Abrikosov, E Snegirev, V M Krivtsun, C J Lee, and F Bijkerk. Extreme ultraviolet (EUV) source and ultra-high vacuum chamber for studying EUV-induced processes. *Plasma Sources Science and Technology*, 24(3):035003, June 2015. doi:10.1088/0963-0252/24/3/035003.

[7] Charles K Birdsall and A. Bruce Langdon. *Plasma physics via computer simulation*. McGraw-Hill, New York, 1985. ISBN 0-07-005371-5 978-0-07-005371-7.

[8] J.W. Gallagher, C. E. Brion, J.A.R. Samson, and P.W. Langhoff. Absolute Cross Sections for Molecular Photoabsorption, Partial Photoionization, and Ionic Photofragmentation Processes. *Journal of Physical and Chemical Reference Data*, 17(1):9–153, 1987. doi:10.1063/1.555821.

[9] R. G. Houlgate, J. B. West, K. Codling, and G. V. Marr. The angular distribution of the 3p electrons and the partial cross section of the 3s electrons of argon from threshold to 70 eV. *Journal of Electron Spectroscopy and Related Phenomena*, 9(2):205–209, 1976. doi:10.1016/0368-2048(76)81030-4.

[10] K. T. Taylor. Photoelectron angular-distribution beta parameters for neon and argon. *Journal of Physics B: Atomic and Molecular Physics*, 10(18):L699, 1977.

[11] Y. M Chung, E. M Lee, T. Masuoka, and James A. R Samson. Dissociative photoionization of H2 from 18 to 124 eV. *The Journal of Chemical Physics*, 99(2):885–889, July 1993. doi:doi:10.1063/1.465352.

[12] James A. R. Samson and G. N. Haddad. Total photoabsorption cross sections of H2 from 18 to 113 eV. *Journal of the Optical Society of America B*, 11(2):277–279, February 1994. doi:10.1364/JOSAB.11.000277.

[13] J. A.R. Samson, L. Lyn, G. N. Haddad, and G. C. Angel. RECENT PROGRESS ON THE MEASUREMENT OF ABSOLUTE ATOMIC PHOTOIONIZATION CROSS SECTIONS. *Le Journal de Physique IV*, 01(C1):C1–99–C1–107, March 1991. doi:10.1051/jp4:1991113.

[14] W. F. Chan, G. Cooper, X. Guo, G. R. Burton, and C. E. Brion. Absolute optical oscillator strengths for the electronic excitation of atoms at high resolution. III. The photoabsorption of argon, krypton, and xenon. *Physical Review A*, 46(1):149–171, July 1992. doi:10.1103/PhysRevA.46.149.

[15] J. B. West and G. V. Marr. The Absolute Photoionization Cross Sections of Helium, Neon, Argon and Krypton in the Extreme Vacuum Ultraviolet Region of the Spectrum. *Proceedings of the Royal Society A: Mathematical, Physical and Engineering Sciences*, 349(1658):397–421, May 1976. doi:10.1098/rspa.1976.0081.

[16] Joseph Berkowitz. *Atomic and molecular photoabsorption: absolute total cross sections*. Academic Press, 2001. ISBN 978-0-08-052769-7.

[17] D. M. P. Holland, K. Codling, G. V. Marr, and J. B. West. Multiple photoionisation in the rare gases from threshold to 280 eV. *Journal of Physics B: Atomic and Molecular Physics*, 12(15):2465, 1979. doi:10.1088/0022-3700/12/15/008.

[18] G. D. Hobbs and J. A. Wesson. Heat flow through a Langmuir sheath in the presence of electron emission. *Plasma Physics*, 9(1):85, 1967.

[19] V. Baglin, J. Bojko, C. Scheuerlein, Oswald Gröbner, M. Taborelli, Bernard Henrist, and Noël Hilleret. The secondary electron yield of technical materials and its variation with surface treatments. Technical Report LHC-Project-Report-433 ; CERN-LHC-Project-Report-433, 2000.

[20] Yinghong Lin and David C. Joy. A new examination of secondary electron yield data. *Surface and Interface Analysis*, 37(11):895–900, November 2005. doi:10.1002/sia.2107.

[21] M. Belhaj, J. Roupie, O. Jbara, J. Puech, N. Balcon, and D. Payan. Electron emission at very low electron impact energy: Experimental and Monte-Carlo results. 2013. doi:10.5170/CERN-2013-002.137.

[22] P. H. Dawson. Secondary Electron Emission Yields of some Ceramics. *Journal of Applied Physics*, 37(9):3644, 1966. doi:10.1063/1.1708934.

[23] T. Tondu, M. Belhaj, and V. Inguimbert. Electron-emission yield under electron impact of ceramics used as channel materials in Hall-effect thrusters. *Journal of Applied Physics*, 110(9):093301, November 2011. doi:10.1063/1.3653820.

[24] Burton L. Henke, Jerel A. Smith, and David T. Attwood. 0.1–10-keV x-ray-induced electron emissions from solids—Models and secondary electron measurements. *Journal of Applied Physics*, 48:1852, 1977. doi:10.1063/1.323938.

[25] David R Lide. *CRC handbook of chemistry and physics, 2003-2004: a ready-reference book of chemical and physical data*. CRC Press, Boca Raton, Fla., 2003. ISBN 0-8493-0484-9 978-0-8493-0484-2.

[26] R. H. Day, P. Lee, E. B. Saloman, and D. J. Nagel. Photoelectric quantum efficiencies and filter window absorption coefficients from 20 eV to 10 KeV. *Journal of Applied Physics*, 52(11):6965–6973, November 1981. doi:10.1063/1.328653.

[27] Kenichi Nanbu. Simple Method to Determine Collisional Event in Monte Carlo Simulation of Electron-Molecule Collision. *Japanese Journal of Applied Physics*, 33(Part 1, No. 8):4752–4753, August 1994. doi:10.1143/JJAP.33.4752.

[28] J. Dutton. A survey of electron swarm data. *Journal of Physical and Chemical Reference Data*, 4(3):577–856, July 1975. doi:10.1063/1.555525.

[29] E. Graham, D. R. James, W. C. Keever, D. L. Albritton, and E. W. McDaniel. Mobilities and longitudi-

nal diffusion coefficients of mass-identified hydrogen ions in H2 and deuterium ions in D2 gas. *The Journal of Chemical Physics*, 59(7):3477–3481, October 1973. doi:doi:10.1063/1.1680505.

[30] John Hornbeck. The Drift Velocities of Molecular and Atomic Ions in Helium, Neon, and Argon. *Physical Review*, 84(4):615–620, 1951. doi:10.1103/PhysRev.84.615.

[31] Rainer Johnsen and Manfred A. Biondi. Mobilities of doubly charged rare-gas ions in their parent gases. *Physical Review A*, 18(3):989–995, September 1978. doi:10.1103/PhysRevA.18.989.

[32] M. S. Mokrov and Yu P. Raizer. Monte Carlo method for finding the ionization and secondary emission coefficients and I–V characteristic of a Townsend discharge in hydrogen. *Technical Physics*, 53(4):436–444, April 2008. doi:10.1134/S1063784208040075.

[33] T. W. Shyn, W. E. Sharp, and Y.-K. Kim. Doubly differential cross sections of secondary electrons ejected from gases by electron impact: 25-250 eV on H2. *Physical Review A*, 24(1):79–88, July 1981. doi:10.1103/PhysRevA.24.79.

[34] M. E. Rudd, K. W. Hollman, J. K. Lewis, D. L. Johnson, R. R. Porter, and E. L. Fagerquist. Doubly differential electron-production cross sections for 200–1500-eV e+H2 collisions. *Physical Review A*, 47(3):1866–1873, March 1993. doi:10.1103/PhysRevA.47.1866.

[35] M. J. Brunger and S. J. Buckman. Electron–molecule scattering cross-sections. I. Experimental techniques and data for diatomic molecules. *Physics reports*, 357(3):215–458, 2002.

[36] T. Šimko, V. Martišovitš, J. Bretagne, and G. Gousset. Computer simulations of H+ and H3+ transport parameters in hydrogen drift tubes. *Physical Review E*, 56(5):5908–5919, November 1997. doi:10.1103/PhysRevE.56.5908.

[37] Hayashi. Bibliography of Electron and Photon Cross Sections with Atoms. 2003.

[38] Arthur V. Phelps. `http://jilawww.colorado.edu/~avp/`.

[39] R. Rejoub, B. G. Lindsay, and R. F. Stebbings. Determination of the absolute partial and total cross sections for electron-impact ionization of the rare gases. *Physical Review A*, 65(4):042713, April 2002. doi:10.1103/PhysRevA.65.042713.

[40] Brent R. Yates and Murtadha A. Khakoo. Near-threshold electron-impact doubly differential cross sections for the ionization of argon and krypton. *Physical Review A*, 83(4):042712, April 2011. doi:10.1103/PhysRevA.83.042712.

[41] A. Fiala, L. C. Pitchford, and J. P. Boeuf. Two-dimensional, hybrid model of low-pressure glow discharges. *Physical Review E*, 49(6):5607, 1994. doi:10.1103/PhysRevE.49.5607.

[42] H. Deutsch, K. Becker, S. Matt, and T. D. Märk. Calculated cross sections for the electron-impact ionization of metastable atoms. *Journal of Physics B: Atomic, Molecular and Optical Physics*, 32(17):4249, 1999.

[43] A. V. Phelps. The application of scattering cross sections to ion flux models in discharge sheaths. *Journal of Applied Physics*, 76(2):747, 1994. doi:10.1063/1.357820.

[44] Kazuhiko Okuno. Charge Transfer of Ar^2+ and Kr^2+ in Their Own Gases Studied by the Beam Guide Technique. *Journal of the Physical Society of Japan*, 55(5): 1504–1515, 1986. doi:10.1143/JPSJ.55.1504.

[45] R. M. van der Horst, J. Beckers, E. A. Osorio, and V. Y. Banine. Exploring the electron density in plasmas induced by extreme ultraviolet radiation in argon. *Journal of Physics D: Applied Physics*, 48(28):285203, 2015. doi:10.1088/0022-3727/48/28/285203.

[46] R M van der Horst, J Beckers, E A Osorio, and V Y Banine. Dynamics of the spatial electron density distribution of EUV-induced plasmas. *Journal of Physics D: Applied Physics*, 48(43):432001, November 2015. doi:10.1088/0022-3727/48/43/432001.